Journal of the Mechanics and Physics of Solids 61 (2013) 597–610

Contents lists available at SciVerse ScienceDirect

Journal of the Mechanics and Physics of Solids

journal homepage: www.elsevier.com/locate/jmps

Adhesion of nanoscale asperities with power-law profiles

David S. Grierson [a,1], Jingjing Liu [a,2], Robert W. Carpick [b], Kevin T. Turner [a,b,*]

[a] Department of Mechanical Engineering, University of Wisconsin, Madison, WI 53706, United States
[b] Department of Mechanical Engineering and Applied Mechanics, University of Pennsylvania, Philadelphia, PA 19104, United States

ARTICLE INFO

Article history:
Received 16 April 2012
Received in revised form
30 August 2012
Accepted 3 September 2012
Available online 17 September 2012

Keywords:
Pull-off force
Single-asperity
Work of adhesion
Power-law profile
Contact mechanics
Adhesion potential

ABSTRACT

The behavior of single-asperity micro- and nanoscale contacts in which adhesion is present is important for the performance of many small-scale mechanical systems and processes, such as atomic force microscopy (AFM). When analyzing such problems, the bodies in contact are often assumed to have paraboloidal shapes, thus allowing the application of the familiar Johnson–Kendall–Roberts (JKR), Derjaguin–Müller–Toporov (DMT), or Maugis–Dugdale (M–D) adhesive contact models. However, in many situations the asperities do not have paraboloidal shapes and, instead, have geometries that may be better described by a power-law function. An M–D-*n* analytical model has recently been developed to extend the M–D model to asperities with power-law profiles. We use a combination of M–D-*n* analytical modeling, finite element (FE) analysis, and experimental measurements to investigate the behavior of nanoscale adhesive contacts with non-paraboloidal geometries. Specifically, we examine the relationship between pull-off force, work of adhesion, and range of adhesion for asperities with power-law-shaped geometries. FE analysis is used to validate the M–D-*n* model and examine the effect of the shape of the adhesive interaction potential on the pull-off force. In the experiments, the extended M–D model is applied to analyze pull-off force measurements made on nanoscale tips that are engineered via gradual wear to have power-law shapes. The experimental and modeling results demonstrate that the range of the adhesive interaction is a crucial parameter when quantifying the adhesion of non-paraboloidal tips, quite different than the familiar paraboloidal case. The application of the M–D-*n* model to the experimental results yields an unusually large adhesion range of 4–5 nm, a finding we attribute to either the presence of long-range van der Waals forces or deviations from continuum theory due to atomic-scale roughness of the tips. Finally, an adhesion map to aid in analysis of pull-off force measurements of non-paraboloidal tips is presented. The map delineates the cases in which a simplified rigid analysis can be used to analyze experimental data.

1. Introduction

Adhesive forces that act between bodies in contact play a crucial role in determining the behavior of small-scale mechanical systems that have high surface-area-to-volume ratios. For example, the performance of tools designed to

* Corresponding author at: University of Pennsylvania, Department of Mechanical Engineering and Applied Mechanics, 220 S. 33rd St, 245 Towne Building, Philadelphia, PA 19104-6315, United States. Tel.: +1 215 573 7485; fax: +1 215 573 6334.
E-mail address: kturner@seas.upenn.edu (K.T. Turner).
[1] Now with systeMECH, LLC, Madison, WI 53703, United States.
[2] Now with Applied Materials, Inc., Santa Clara, CA 95054, United States.

0022-5096/$ - see front matter © 2012 Elsevier Ltd. All rights reserved.
http://dx.doi.org/10.1016/j.jmps.2012.09.003

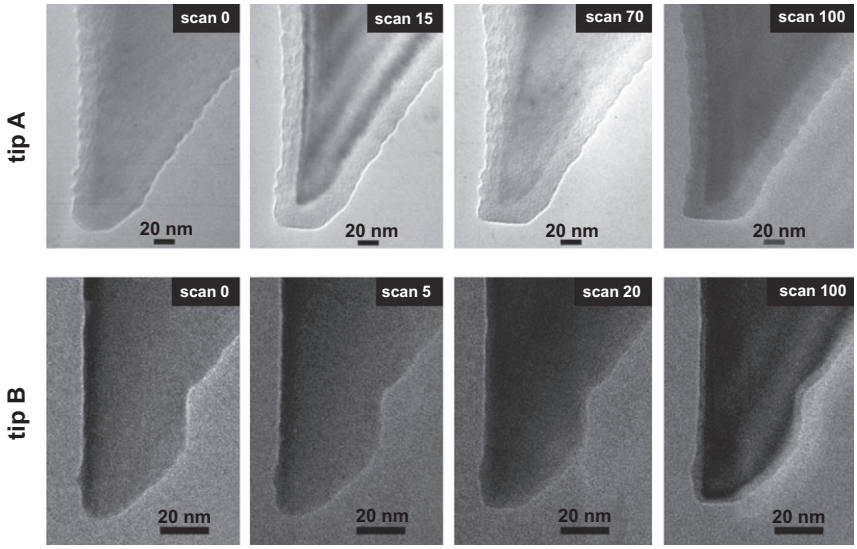

Fig. 1. TEM images showing the evolution of a DLC-coated Si AFM tip (tip A) and a Si AFM tip (tip B) due to scanning via AFM across a flat DLC surface. The scanning distance each tip was subjected to is equal to the scan number multiplied by 5.12 mm.

image and manipulate matter at the nanoscale through probing with a tip, such as atomic force microscopy (AFM), depends critically on the adhesion and friction between the tip and sample. The increased use of tip-based probes in demanding applications, including nanomechanical data storage (Gotsmann and Lantz, 2008; Wiesmann et al., 2009), nanomanufacturing (Gozen and Ozdoganlar, 2010; Malshe et al., 2010), high-rate imaging (Lee et al., 2012), and nanometrology (Ukraintsev and Banke, 2010), has led to a critical need to better characterize and understand the adhesion behavior of nanoscale tip-sample contacts. Tip-based metrology and manufacturing techniques rely on controlled nanoscale tip-sample contacts, and characterizing the geometries and adhesion properties of these contacts is essential for understanding their performance. For example, adhesive forces alone can cause significant local stresses in AFM tips that can lead to substantial wear and tip degradation (Liu et al., 2010a, 2010b).

An AFM tip in contact with a sample is typically viewed as a paraboloid in contact with a flat surface. With this assumption, the behavior of the tip-sample contact can be examined using adhesive contact theories, such as DMT (Derjaguin et al., 1975) and JKR (Johnson et al., 1971), which extend the Hertzian contact model to include adhesion. These models are routinely used to extract adhesion energies from pull-off force measurements conducted with AFM and to analyze stresses and deformation in tip-sample contacts. However, AFM tips are often not paraboloidal in shape and may have more complex geometries as a result of the fabrication method used to make the tip or due to wear that occurs during use. In particular, tips often have slightly flattened apexes, meaning that their geometry may be better described by a power-law function with an exponent greater than two. Fig. 1 shows examples of AFM tips that exhibit flattened tip geometries as a result of being scanned across a surface under typical imaging conditions. Understanding the behavior of contacts between power-law shaped bodies has received relatively little attention, thus most adhesive contacts in AFM are analyzed assuming a paraboloidal-shaped tip.

The objective of this paper is to investigate the behavior of tip-sample adhesive contacts in which the tip geometry is described by a power-law function. The aim is to provide guidance for analyzing power-law-shaped adhesive contacts and to highlight key differences between power-law-shaped tips and paraboloidal tips. The mechanics of the contacts are examined using an established analytical model for the adhesion of power-law-shaped asperities, referred to as the M–D-*n* model, as well as finite element analysis with traction-separation elements at the interface. The M–D-*n* model assumes a Dugdale traction law, while the finite element analysis is used to investigate the impact of alternate forms of the adhesion potential. Experimentally, a series of AFM pull-off force measurements was performed on tips that evolve from paraboloidal shapes to power-law shapes due to wear (Fig. 1). The M–D-*n* model is used to analyze the experimental measurements, and limitations and challenges of analyzing power-law-shaped tips are identified.

2. Background

Parameters of particular importance in characterizing tip-based contacts are the size and shape of tip, the elastic properties of the tip and sample, and the adhesion present at the tip-sample interface. The geometries of tips used in atomic force microscopy (AFM) can be characterized using several direct and/or indirect imaging approaches. Scanning electron microscopy (SEM) and transmission electron microscopy (TEM) imaging, for example, can provide a direct image of the tip. The tip geometry can also be determined indirectly by imaging a tip-characterization sample and subsequently analyzing the resulting images using statistical or deconvolution algorithms (Bloo et al., 1999; Chung and Kim, 2003, 2007;

Gotsmann and Lantz, 2008; Katsuki et al., 2002; Larsen et al., 2002; Liu et al., 2010b; Maw et al., 2002; Villarrubia, 1997). To quantify the interfacial adhesion between the tip and the sample, measurements of the maximum adhesive force required to separate the tip-sample junction (denoted the pull-off force) are often taken. Pull-off force measurements are conducted in a wide variety of settings in order gain an understanding of the interaction forces that control the mechanical responses of natural and engineered interfaces at the nanoscale. The measurements of tip geometry and pull-off force, along with the elastic properties of the tip and sample, can be used in an appropriate contact mechanics model to calculate the adhesive properties of the tip-sample interface. In these measurements, the adhesion is typically described by a single value: the work of adhesion. Of course, the validity of the calculated adhesion is highly dependent on the degree to which the experimental situation matches the assumptions in the theoretical model used to examine the mechanics.

There is extensive published work describing continuum adhesive contact mechanics models. Previous work has largely been focused on quantifying adhesion between smooth paraboloidal tips and smooth surfaces. The non-adhesive contact mechanics analysis of Hertz was extended to include adhesion by Johnson, Kendall, and Roberts (JKR) (Johnson et al., 1971) and Derjaguin, Müller, and Toporov (DMT) (Derjaguin et al., 1975); both groups separately derived distinct expressions relating the work of adhesion to the pull-off force and the radius of curvature of a paraboloidal tip in adhesive contact with a surface. The JKR approach is generally more appropriate when the surface forces act over a short range, and the contacting bodies are larger and compliant. In contrast, the DMT model is generally better suited for cases in which the surfaces forces are long-range, and the contacting bodies are smaller and stiffer. The Maugis–Dugdale (M–D) model unified the theories of JKR and DMT and quantitatively describes the transition between the two. Maugis demonstrated the transition by considering the adhesive interaction to be described by a simple Dugdale (i.e., square-well) potential, which is defined in terms of two parameters: the work of adhesion and either the strength or range of adhesion (Maugis, 1992). The non-dimensional Maguis parameter can be used to quantify the transition from the JKR limit to the DMT limit (Maugis, 1992). In addition to paraboloidal tip shapes, analytical adhesive contact models for spherical tips (Greenwood, 2009; Maugis, 1995; Yao et al., 2007) and flat-ended indenters (Gao and Yao, 2004; Persson, 2003; Tian and Chung-Yuen, 2005) have also been reported. Contacting bodies with a geometry described by a power-law function have been considered using a JKR-like model (Carpick et al., 1996a, 1996b) and recently using a Maugis–Dugdale model (Zheng and Yu, 2007). Zheng and Yu (2007) provide a model for DMT-like to JKR-like adhesion behavior for power-law-shaped tips (referred to as the M–D-n model) that is used extensively in the present work.

These adhesive contact-mechanics models have been used to calculate the work of adhesion between tips and samples from pull-off forces measured using AFM in a number of experimental studies (Cho et al., 2004; Drelich et al., 2004; Giesbers et al., 2002; Grierson et al., 2005; Han et al., 2009; Jacquot and Takadoum, 2001; Jallo et al.,; Liu et al., 2005, 2010b; Singh and Whitten, 2008; Stiess et al., 2004; Sumant et al., 2005; Tormoen et al., 2004). Common practice is to use the DMT, JKR or M–D solutions to calculate the work of adhesion using the measured force and the tip radius determined by fitting the shape of the tip to a paraboloid. This approach is limited by the constraint that the tip is a smooth paraboloid, and results can vary significantly if the tip's shape is either initially non-paraboloidal, exhibits appreciable roughness, or, during use, changes from the assumed paraboloidal form due to wear or plastic deformation. The recently developed M–D-n model has the potential to accommodate a wider range of experimental tip geometries. However, this model has not yet been applied to experimental data, and systematic experimental measurements of adhesion of power-law shapes tips have not been reported.

3. Experimental and analytical methods

3.1. Analytical M–D-n model

A broad range of AFM tip shapes can be described by a power-law function that defines the tip profile, $z(r)$, as

$$z(r) = \frac{r^n}{nQ}, \tag{1}$$

where r is the radial coordinate, n is the power index, and Q is a parameter related to the curvature of the tip. When $n=2$, for example, the power-law function describes a paraboloid with radius R, and $Q=R$. Here we elect to define Q as $S^{n-2}R^{n-1}$ to simplify subsequent discussions without loss of generality. With this change, R has units of length regardless of the index n, S is a non-dimensional parameter that describes the steepness of the power-law profile, and Eq. (1) becomes

$$z(r) = \frac{r^n}{nS^{n-2}R^{n-1}}. \tag{2}$$

In the case of $n=2$ (i.e., a paraboloid), the value of S has no effect on the function.

Zheng and Yu (2007) present a Maugis–Dugdale type adhesive model that examines the adhesive, frictionless contact of elastic bodies with power-law shapes with any power index n across the DMT-like to JKR-like range of adhesive behavior (subsequently referred to as the M–D-n model). A Dugdale adhesive traction-separation law assumes that the adhesive stress, σ_0, is constant over a separation range from 0 to h (henceforth referred to as the adhesion range). The product of the

adhesive stress and adhesion range is equal to the work of adhesion, W_A:

$$W_A = \sigma_0 h. \tag{3}$$

The M–D-n equations given by Zheng and Yu (2007) can be solved numerically to determine the contact radius, a, and displacement, δ, based on the applied load, P, and work of adhesion for a power-law tip with defined geometry and elastic properties. Non-dimensional forms of a, δ, and P are

$$\tilde{a} \equiv \frac{a}{(Q^2 W_A E^{*^{-1}})^{1/(2n-1)}}, \tag{4}$$

$$\tilde{\delta} \equiv \frac{\delta}{(Q {W_A}^n E^{*^{-n}})^{1/(2n-1)}}, \tag{5}$$

$$\tilde{P} \equiv \frac{P}{\pi(Q^3 {W_A}^{n+1} E^{*^{n-2}})^{1/(2n-1)}}, \tag{6}$$

where E^* is the reduced elastic modulus:

$$\frac{1}{E^*} = \frac{1-\nu_1^2}{E_1} + \frac{1-\nu_2^2}{E_2}. \tag{7}$$

A generalized transition parameter Λ (analogous to the familiar Maugis parameter, λ, Maugis, 1992) that characterizes the degree of deformation due to adhesion and describes the transition from JKR-like to DMT-like behavior for power-law-shaped elastic bodies in contact is defined as (Zheng and Yu, 2007)

$$\Lambda = \sigma_0 (Q {W_A}^{1-n} E^{*^{-n}})^{1/(2n-1)}. \tag{8}$$

The non-dimensional displacement and load are related to the adhesive properties, contact radius, and tip shape and elastic properties by (Zheng and Yu, 2007)

$$\tilde{\delta} = \frac{1}{2} B\left(\frac{n}{2}, \frac{1}{2}\right) \tilde{a}^n - 2\Lambda\tilde{a}\sqrt{m^2-1}, \tag{9}$$

$$\tilde{P} = \frac{1}{\pi} B\left(\frac{n}{2}+1, \frac{1}{2}\right) \tilde{a}^{n+1} - \frac{2}{\pi}\Lambda\tilde{a}^2(m^2 \operatorname{arcsec}(m) + \sqrt{m^2-1}), \tag{10}$$

where B is the Euler beta function (Frank et al., 2010), and the parameter m is the radial distance over which the adhesive stresses act on the body divided by the contact radius. To solve the adhesive contact problem, the Griffith criterion $G = W_A$ must be satisfied, where G is the strain energy release rate. Imposing this condition results in the following dimensionless equation (Zheng and Yu, 2007):

$$\frac{1}{n}\Lambda\tilde{a}^n\left[m^n\left(1 - I_{m^{-2}}\left(\frac{n+1}{2}, \frac{1}{2}\right)\right) - \frac{n}{\pi} B\left(\frac{n}{2}, \frac{1}{2}\right)\operatorname{arcsec}(m)\right] + \frac{4}{\pi}\Lambda^2\tilde{a}(\sqrt{m^2-1}\operatorname{arcsec}(m) + 1 - m) = 1, \tag{11}$$

where I_x is the regularized beta function (Frank et al., 2010). Eq. (11) is essentially used to determine the value of the parameter m. Therefore to determine a, δ, and P for an experimental AFM measurement, the following steps are required. First, the values for E^*, n, Q, W_A, and σ_0 (or h) that describe the elastic, geometric, and adhesive properties, respectively, of the tip-sample junction are selected. While Q and n, can be determined experimentally, and values for E^* are available using reference values, W_A and σ_0 (or, equivalently, h) are simply not known *a priori*, and thus assumed values must be used. Second, Eq. (8) is used to calculate the transition parameter Λ. Third, the value of m that satisfies Eq. (11) is solved numerically as a function of $\tilde{a}$, where $\tilde{a}$ is systematically varied over a physically reasonable range. Fourth, $\tilde{P}$ and $\tilde{\delta}$ are calculated from the calculated m and $\tilde{a}$ values using Eqs. (9) and (10), respectively. Lastly, Eqs. (4)–(6) are used to determine a, δ, and P. The force required to separate the power-law-shaped tip from a flat surface (i.e., the pull-off force, F_P) is taken as the maximum value of P achieved during pull-off. If, conversely, the pull-off force is known and the work of adhesion is the parameter of interest, then one must use the above procedure to iterate over a range of W_A until the measured pull-off force is determined.

3.2. Analysis of rigid power-law-shaped tips

DMT contact mechanics is frequently used to calculate the work of adhesion from F_P values that are experimentally measured for a wide range of tip-sample contact pairs that can be described as paraboloids (e.g., Cho et al., 2004; Giesbers et al., 2002; Han et al., 2009; Jacquot and Takadoum, 2001; Jallo et al.,; Singh and Whitten, 2008; Stiess et al., 2004; Tormoen et al., 2004). If a Dugdale interaction potential between a paraboloidal tip and a flat surface is considered, the DMT relation of $F_{P\text{-}DMT} = 2\pi W_A R$ can be obtained by treating both the tip and sample as being rigid and simply integrating the adhesive stresses over the surface of the tip. This treatment of the contacting bodies as being rigid to obtain $F_P = 2\pi W_A R$ is often referred to as the "Bradley limit" (Greenwood, 1997). For tip-sample contacts that experience a small amount of deformation due to adhesion (e.g., paraboloidal tip-sample contacts with a Maugis parameter $< \sim 0.1$), the expression

relating F_P to W_A, can be determined for any form of interaction potential by integrating the adhesives stresses over the surface of the tip. This approach is considerably simpler than the M–D-n model described above and is useful and essential for analyzing experimental data in certain situations. The pull-off force calculated via this rigid approximation is denoted as F_{P-r}.

For a power-law-shaped tip with a Dugdale adhesive traction law, the pull-off force determined from the rigid approximation is

$$F_{p-r\ \ Dug} = \frac{W_A}{h}\pi(nhQ)^{2/n}. \tag{12}$$

When $n=2$, and taking $Q=R^{n-1}$ (i.e., $S=1$), Eq. (12) reduces to the DMT pull-off force. Note that for paraboloid tips, $n=2$, the pull-off force is independent of h, but for profiles described by larger power indices, $n>2$, the pull-off force is a function of h. Thus, for $n=2$ tips, W_A alone defines the adhesion when determining the pull-off force, while for tips with $2n\neq 2$ both W_A and h are needed to define the interaction potential when calculating the pull-off force. In Section 4, the dependence of F_P on both W_A and h is explored using both the rigid approximation and a finite element (FE) approach for several cases: a Dugdale potential, a Lennard–Jones potential, and two triangular potentials. The FE results are used to establish the range of validity of this rigid approximation.

3.3. Finite element analysis

To simulate frictionless contact between an elastic tip and a flat surface in the presence of adhesion described by various interaction potentials, a 2-D axisymmetric FE model was used. The profile of the tip was defined by a power-law function, and the tip geometry was meshed using 2-D 8-node axisymmetric elements. The exact number of elements in the tip varied as the geometry of tip was changed in the study, however all models had more than 7566 elements in the tip. The selected mesh density was determined via a convergence study. For all simulation results presented here, elastic constants $E=150$ GPa and $\nu=0.3$, which are representative of the properties of stiff AFM tips made of silicon (Si) or diamond-like carbon, were used. The flat surface was modeled as a frictionless and rigid plane. Thus, the E^* for all the FE calculations is 164.8 GPa. A rigid counter surface was used to simplify the model and reduce computation time, however the results here would also apply to two elastic bodies in contact that have the same E^*. The analytical model in Section 3.1 can be used to assess the effect of varying E^*. The adhesive tractions between the surface and the tip were represented using nonlinear spring elements. The spring elements were connected between the nodes on the surface of the tip and nodes fixed below the rigid plane and only provided a force in the direction normal to the surface. The effective width (i.e., spacing) of the spring-based traction-separation elements at the interface varied from 0.2 to 0.35 nm across the different cases examined; the number of elements depends on the width of the particular model. The element width at the interface was determined through a convergence study. To model a specific interaction potential using the spring elements, the exact traction-separation relationship of interest was set for each nonlinear spring. The power-law-shaped tips were separated from the rigid plane in displacement control in order to avoid any snap-off instabilities, and F_P was measured as the maximum adhesive load experienced by the tip during the pull-off process. The nodes and elements that comprised the FE model were generated using a custom script written in Matlab, and the simulations were carried out with the commercial software package Abaqus (Dassault Systèmes, Vélizy-Villacoublay, France).

3.4. Experimental

Two different AFM probes were used in experiments: (1) a single-crystalline Si AFM probe with an integrated etched Si tip (Nanosensors, Neuchatel, Switzerland, type: NCHR), (2) an identical silicon probe coated with a thin diamond-like carbon (DLC) film. The uncoated Si tips were initially scanned across ultrananocrystalline diamond surfaces (Advanced Diamond Technologies, Romeoville, IL), which are hard, randomly rough surfaces with a typical surface roughness of $\sim$9 nm r.m.s. over a $1\times 1\ \mu m^2$ area, to intentionally wear the extremely sharp Si tips (initial radius <5 nm) into smooth, paraboloidal tips with a radius of $\sim$10 nm. The slight blunting of the tip helps to avoid tip fracture during testing. One pre-shaped Si tip was coated with $\sim$20 nm of DLC using a plasma immersion ion implantation and deposition (PIIID) technique with an acetylene plasma at a pressure of 12 mTorr and a 5 kV applied bias (Bares et al., 2007). The DLC-coated tip had an average radius of curvature of $\sim 30\ nm \pm 3$ nm.

After the AFM tips were prepared as described above, the geometries of both the Si and DLC tips were systematically changed through wear experiments in which the tips were raster scanned in contact mode across a DLC surface (roughness $\sim$1 nm r.m.s., also grown using the same PIIID method) using a Veeco Multimode AFM. A total of 100 $5\times 5\ \mu m^2$ contact-mode images were acquired with 512 scan lines per image. Each image corresponds to a linear scan distance of 5.12 mm, leading to a total scan distance of 512 mm. All scans were performed at a speed of 29.7 μm/sec, with zero externally applied load (i.e., zero cantilever deflection), and in a controlled environment with a relative humidity (RH) of 13% and a N_2 background. At certain scan intervals, the tip geometries were characterized using two techniques – inverse AFM imaging and direct imaging using TEM (Liu et al., 2010b). Inverse imaging by scanning the AFM tips across a Nioprobe® (Aurora NanoDevices Inc., Nanaimo, BC Canada) surface, which consists of many small high aspect ratio features, was done to assess the 3D geometries of the apexes of the tips based on convolution/deconvolution theory (Villarrubia, 1997). A TEM

(JEOL 100CX) was used to acquire side-view images of the tips, with the tips being viewed in the direction perpendicular to the long axis of the AFM cantilever. The pull-off force, F_P, between each tip and the sample surface was measured after various scan distances during the test. The pull-off force was taken to be the maximum adhesive force experienced during retraction, and is calculated as $F_P = k\Delta$, where k is the stiffness of the AFM cantilever, and Δ is the maximum cantilever deflection measured during retraction. This maximum deflection is reached just as a pull-off instability occurs. It is universally observed that pull-off occurs at or near the maximum adhesive force since the typical stiffness of the cantilevers used here, and in most contact-mode AFM experiments, are small (< 1 N/m) compared to the slope of typical tip-sample interaction potentials shortly beyond their minimum value (Bhushan, 2004). In fact, with relatively stiff cantilevers, the pull-off instability occurs after the maximum adhesive force is reached during retraction (i.e., at a lower force value than the maximum adhesive force). That behavior is not observed in our experiments. Thus, the pull-off force obtained in our experiments is indistinguishable from the maximum adhesive force obtained from either the finite element analysis or the analytical model. The stiffness of each cantilever was calibrated using a reference lever of known stiffness (Tortonese and Kirk, 1997).

4. Results and discussion

4.1. Experimental results and analysis

TEM images of two AFM tips, one DLC-coated Si (tip A) and one Si (tip B), that were collected at various intervals over the 512 mm wear scans are shown in Fig. 1. The lighter contrast layer on tip A is the amorphous DLC coating; the lighter contrast thin layer on tip B is a native oxide (SiO_x). Both tips demonstrate gradual wear and flattening at the tip apexes over the course of the wear tests. Since the DLC counter surface is extremely smooth (RMS roughness ~ 1 nm), both tip apexes become flattened due to wear. The tip shapes evolved into geometries that are well described by power-law functions with higher-order indices ($n = 4$–6). This gradual engineering of the tip shape due to the wear process allows us to investigate the adhesion mechanics of tips with shapes that are more complicated than the conventional paraboloidal shape. As shown in the upper row of Fig. 1, wear of tip A only occurs in the DLC coating, which means that the contact interface for tip A remains self-mated throughout the duration of the wear test. The flattening of the tip apexes of both tips are apparent in the AFM images shown in Fig. 2 when comparing the Nioprobe images taken at scan 0 and scan 100. An AFM topography image of a surface is the convolution of the tip shape with the topography of the surface. Since the Nioprobe surface is composed of randomly arranged sharp spikes (spike radii < 5 nm), the AFM image of a Nioprobe sample essentially depicts multiple inverse images of end of the AFM tip. The qualitative observations of the AFM images agree well with the TEM imaging results: tips A and B, which have different initial radii (with tip B initially sharper than tip A), become flattened due to the wear process.

As TEM imaging only allows a 2D projection of the tip to be obtained, a key use of Nioprobe images is to assess the 3D shape of the tip apex. The features in the Nioprobe AFM images of Fig. 2a and c resemble paraboloids, and the elevated features in Fig. 2b and d resemble circular plateaus. The fact that these features appear circular across all images suggests that the apices of the AFM tips were largely axisymmetric initially and maintained axial symmetry over the course of the wear tests. The observed axisymmetry of the features is not surprising given the nominal conical geometries of etched AFM tips. Thus, the images of Fig. 2a and c suggest that the tips' 3D shapes can be treated as axisymmetric versions of the 2D projections determined via TEM. Finally, we note that tip axisymmetry as wear occurs has also been demonstrated via blind tip reconstruction in previous AFM wear tests (Liu et al., 2010b).

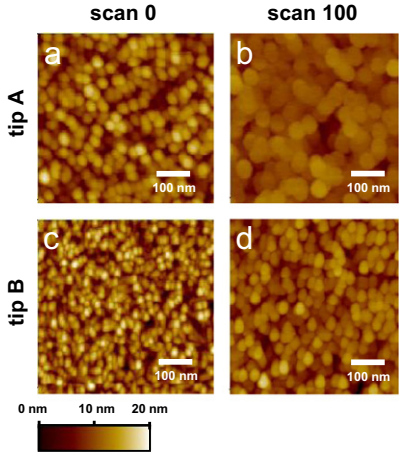

Fig. 2. AFM images of a Nioprobe® tip-characterization sample scanned by tip A and tip B before and after acquiring 100 $5 \times 5\ \mu m^2$ contact-mode images on a flat DLC surface.

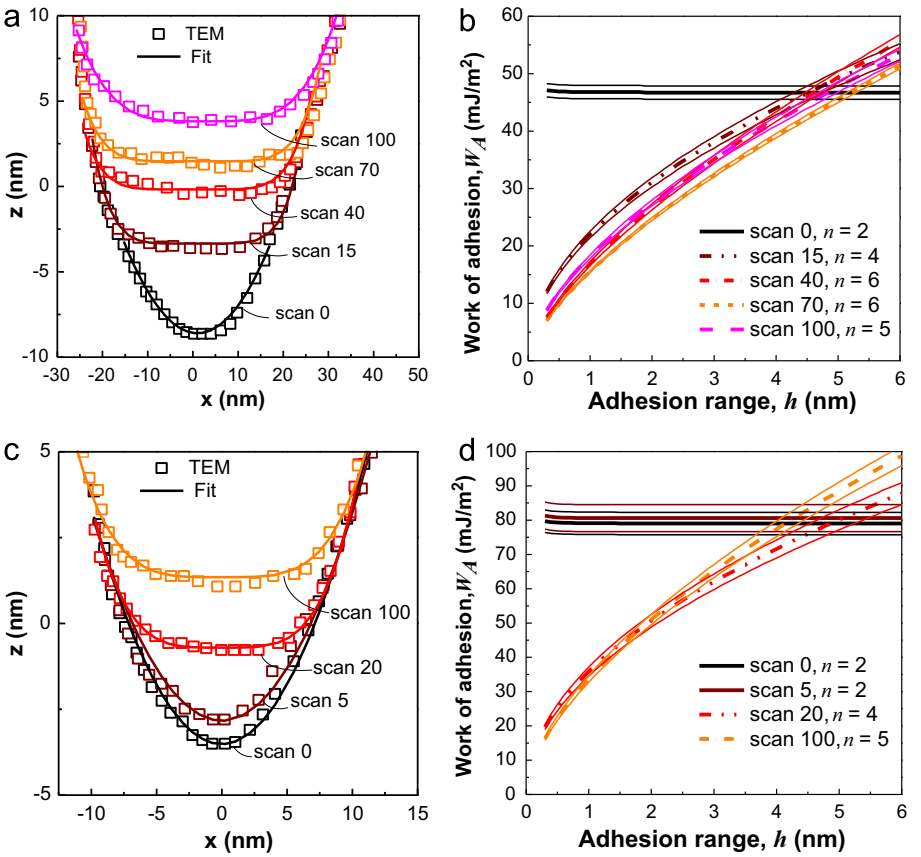

Fig. 3. (a) Profile data from TEM images (squares) and power-law fits (solid lines) to tip A at different scan intervals. (b) Calculated work of adhesion values between tip A and the DLC counter surface as a function of the adhesion range using the M–D-n model (thick solid and dashed lines). Solid thin lines reflect the uncertainties in the calculations. (c) Profile data from TEM images (squares) and power-law fits (solid lines) to tip B at different scan intervals. (d) Calculated work of adhesion values between tip B and the DLC counter surface as a function of adhesion range using the M–D-n model (thick solid and dashed lines). Solid thin lines reflect the uncertainties in the calculations.

The profiles of the AFM tips were extracted from the TEM images, and those profiles were then fit using the general power-law function (Eq. (1)) in a least-squares fashion up to a tip height of 6 nm (Fig. 3a and c). As shown in Fig. 3a and c, both tips evolved from initial paraboloids to shapes that can be described by power-law functions with higher indices (n=3–6). The power-law fits have excellent agreement with the TEM measured profiles for both tips, with fitting errors less than 2%. For the subsequent analysis, the power-law fits were taken to be accurate representations of the tips' geometries, an idealization which excludes the local texture (i.e., roughness) of the tips (Luan and Robbins, 2005; Mo et al., 2009), but represents their overall shapes with a resolution of ~0.5 nm.

The parameters n and Q obtained from the fits, as well as measured pull-off forces and known values for E^* (based on the elastic properties of both the tip and substrate), were used to numerically solve for work of adhesion, W_A, as a function of the assumed adhesion interaction range, h, using the M–D-n Eqs. (4)–(11) (Fig. 3b and d). As shown by the solid lines in Fig. 3b and d, the calculated results for the work of adhesion for both paraboloidal (i.e., initial) tip shapes are nearly independent of adhesion range, even down to a small adhesion range of h=0.3 nm, with only a slight increase noticeable with $h<0.5$ nm. For the DLC tip, the work of adhesion is 46.7 ± 1.5 mJ/m^2; for the Si tip, the work of adhesion is 79.8 ± 3.4 mJ/m^2. These values are consistent with the DMT model, namely $W_A=F_P/2\pi R$. A simple calculation of the Maugis parameter, μ, (Maugis, 1992) confirms that the DMT model is the appropriate choice for quantifying the work of adhesion for these paraboloidal tips if $h\geq0.3$ nm ($\mu<0.1$ for both DLC-DLC and Si-DLC contacts studied here); with $h<0.3$ nm, the Maugis–Dugdale model would be more appropriate.

In contrast to the results for paraboloidal tips, the work of adhesion extracted from pull-off forces of the flattened tips ($n>2$) is strongly dependent on h. Zheng and Yu (2007) noted the important role that h plays in determining the expected pull-off force for tips with power-law shapes, thus the results presented here are not surprising. The adhesion range, h, is difficult to measure experimentally, and, perhaps more significantly, its physical meaning depends on the exact form of the adhesion potential, which is also difficult to measure experimentally. A common assumption is to take h to be on the order

of the equilibrium spacing between strongly bonded atoms (~0.3–0.5 nm) (Gao and Yao, 2004; Persson, 2003). However, this may not be accurate when considering the multiple adhesive interactions between surfaces (including van der Waals attraction, capillary forces, and electrostatic attractions).

For the purpose of understanding and interpreting the data presented in Fig. 3, we assume that the work of adhesion is constant over the course of the wear test, and we determine the work of adhesion from the measurements on initial paraboloidal-shaped tips since a precise value of h is not required when $n=2$. Our assumption of a constant work of adhesion is supported by: (1) the TEM observations that the material present at the tip apexes (either DLC or SiO_x) remains the same throughout the wear test and (2) previous experimental results that demonstrated the consistency of W_A for similar material pairs under similar sliding conditions (Liu et al., 2010b). The h for the adhesion interaction can be estimated by determining the value of h for each tip that yields a constant work of adhesion for the different worn geometries. Graphically, this corresponds to where the curves intersect each other in Fig. 3b and d. For both the DLC (Fig. 3b) and Si (Fig. 3d) tips, the adhesion range, h, is within the range of 4–5 nm. This is much larger than the commonly assumed h values of 0.2–0.5 nm (i.e., short-range atomic bond distances). As mentioned above and reported in the literature (Leite and Herrmann, 2005), adhesion ranges on the order of nanometers are physically possible. For example, longer range electrostatic and van der Waals forces can be significant at separation distances of several nanometers (Cappella et al., 2005; Leite and Herrmann, 2005), and forces between hydrophobic surfaces have been measured out to separation distances of 5–100 nm (Lin et al., 2005). The large adhesion range determined here could also be due to the use of an idealized model that does not capture the atomic details of the tip, for example the atomic-scale roughness. Further study is certainly needed to fully understand the physical origins of these observed long-range interactions. These results do, however, make it clear that knowledge of the adhesion range is essential when interpreting pull-off force measurements of non-paraboloidal tips.

4.2. Dugdale analysis of power-law-shaped tips

The Dugdale adhesion interaction assumed in the analytical M–D-n model is among the simplest interactions one can consider when analyzing tip-sample contacts. Here, we compare the results of three different analyses of pull-off force that assume a Dugdale traction-separation law: (1) the M–D-n model (Section 3.1), (2) the rigid approximation (Section 3.2, Eq. (12)), and (3) the FE-model (Section 3.3).

Fig. 4a and d shows the profiles of the tips considered to compare the different calculations – the geometries are defined by Eq. (2) with the values shown in the figure. Two different values for R ($R=30$ nm and $R=10$ nm) were chosen as representative values that span the range of AFM tip sizes typically encountered in experiments, and the power index, n, was varied from 2 to 5 to investigate how gradual flattening of the tip can change the pull-off force. For the tips with $R=30$ nm, $S=1$ was chosen to set the slopes of all profiles equal to one another at a height 15 nm above the apex of the $n=2$ profile. For the tips with $R=10$ nm, $S=2$ was chosen to set the slopes of the profiles equal to one another at a height of 20 nm above the apex of the $n=2$ profile. In all cases, the work of adhesion was taken as 0.1 mJ/m^2, and the adhesion range was varied from 0.3 to 6 nm. The FE results (denoted as $F_{P\text{-}FE\ Dug}$), the rigid approximation of pull-off force, $F_{P\text{-}r\ Dug}$, and the M–D-n model (denoted as $F_{P\text{-}M\text{-}D\text{-}n}$) were compared over a range of h values.

Excellent agreement was found between the FE results and the M–D-n analytical solution for all cases studied (Fig. 4b and e). There is $<3.5\%$ error between $F_{P\text{-}FE\ Dug}$ and $F_{P\text{-}M\text{-}D\text{-}n}$ across the h, n, and (R, S) values tested, thus verifying the FE modeling approach. The results in Fig. 4 also show that the rigid approximation, $F_{P\text{-}r\ Dug}$, is in very good agreement with the pull-off forces predicted by the M–D-n and FE models. The error between $F_{P\text{-}M\text{-}D\text{-}n}$ and $F_{P\text{-}r\ Dug}$ is $<3.5\%$, with the error only exceeding 2% when $h<0.4$ nm (Fig. 4c and f). This observation indicates that for many practical cases, the simple analytical rigid approximation may be sufficient to analyze experimental data.

To further facilitate the identification of situations in which the rigid solution can be used instead of the full M–D-n solution, we present a map (Fig. 5) to determine whether or not the simple rigid approximation provides an accurate relationship between the pull-off force and the work of adhesion. The map was generated by comparing F_p values calculated using both the M–D-n model and the rigid approximation (Eq. 12) over a wide range of experimentally relevant values of the non-dimensional ratios R/h and σ/E^*. The region in which the rigid approximation is valid (denoted as the rigid regime) is defined as the situations in which the percent difference between $F_{P\text{-}M\text{-}D\text{-}n}$ and $F_{P\text{-}r\ Dug}$ is less than 5%. When plotted as R/h versus σ/E^* on a log–log scale, the boundaries of the rigid regime are straight lines, and there is a separate set of boundaries for each unique value of n. The generalized transition parameter, Λ, defined in Eq. (8), is constant along each boundary line. A second-order polynomial fit ($R^2=0.9999$) that gives $\Lambda_{\text{boundary}}$ (n) as a function of n is

$$\Lambda_{boundary}(n) = -0.002194\, n^2 + 0.067185\, n + 0.022056. \tag{13}$$

If the value of Λ for the experimental case is less than $\Lambda_{\text{boundary}}$ then the rigid approximation can be used. The boundaries are found to cross one another and are within one decade of each other for both the ordinate and abscissa of the plot, meaning the dependence of the boundary on n is not dramatic.

Four example cases (black circle and square markers) are plotted along with the boundaries on the map in Fig. 5 to demonstrate how experimental results can be visualized on the map. The parameters chosen to represent experimentally reasonable conditions in the four cases were $E^*=78$ GPa ($E_1=E_2=150$ GPa, $\nu_1=\nu_2=0.2$), $R=10$ and 40 nm ($S=1$), and $W_A=0.1$ and 1 J/m^2. Example values of h were chosen to be 4, 3, 2, 1, and 0.3 nm. As shown in Fig. 5, when $W_A=0.1$ J/m^2,

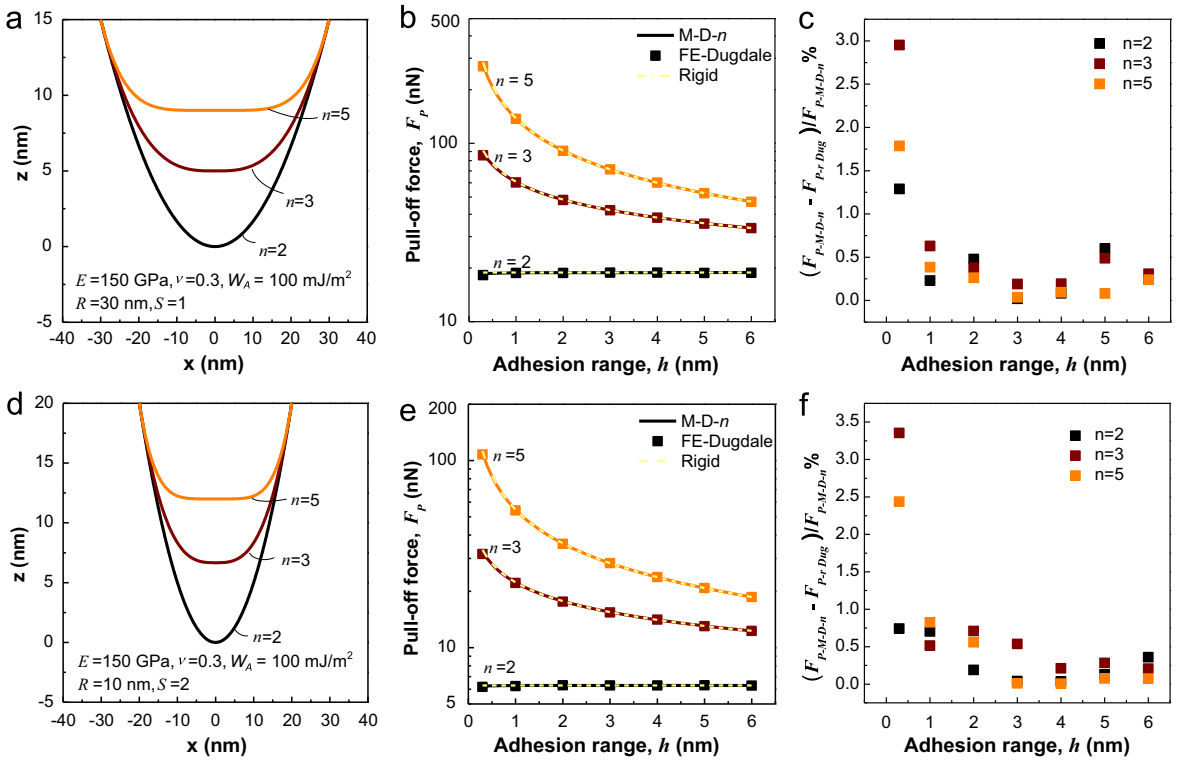

Fig. 4. (a) Profiles of representative power-law tips considered, all with $R=30$ nm. (b) M–D-n results (solid line) compared to the FE results (squares) and the rigid results (dashed line) for pull-off force as a function of adhesion range for the tip shapes shown in (a). Percent difference between the M-D-n results and the rigid results in (b). (d) Profiles of representative power-law tips considered, all with $R=10$ nm. (e) M–D-n results compared to the FE results and the rigid results for pull-off force as a function of adhesion range for the tip shapes shown in (d). Percent difference between the M-D-n results and the rigid results in (e).

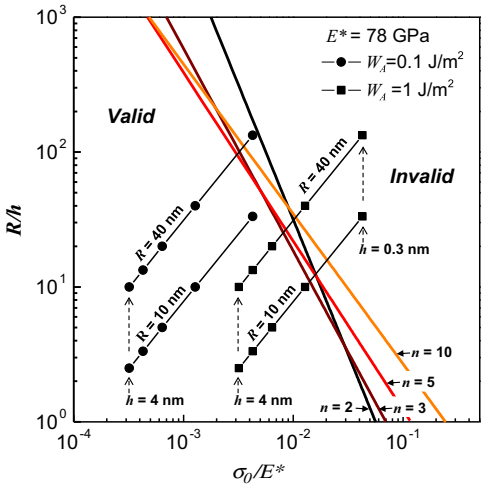

Fig. 5. Map depicting the region in R/h and σ_0/E^* parameter space where the rigid approximation for calculating the pull-off force of a power-law-shaped tip is valid. Black lines show four example cases that demonstrate how the location on the map changes as h decreases when R, W_A, and E^* are assumed to be constant.

the rigid approximation is valid for all values of h shown when the tip is paraboloidal (i.e., $n=2$). With $W_A=0.1$ J/m^2 and $n>2$, the rigid approximation fails to be valid when $h<0.4$ nm for $R=40$ nm. When $W_A=1$ J/m^2, the rigid approximation fails to be valid for a larger range of h values (for example, when $h<1.6$ nm for $R=40$ nm and when $h<0.9$ nm for $R=10$ nm).

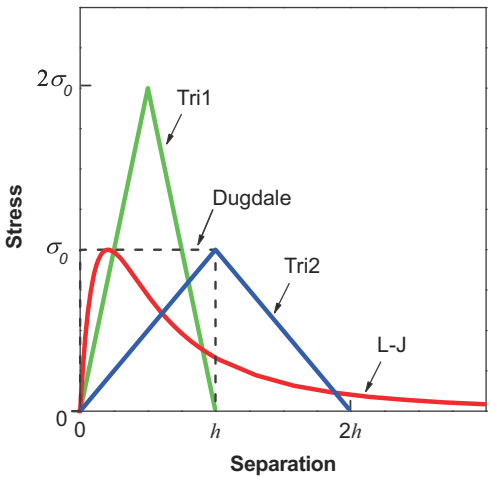

Fig. 6. Plots of the Dugdale, Lennard–Jones, and two triangular (denoted Tri1 and Tri2) interaction potentials considered.

For a given experimental situation, the procedure for determining whether or not the rigid approximation is valid is as follows: (1) measure F_p, R, E^*, and n; (2) solve Eq. (12) to determine W_A as a function of the unknown h; (3) calculate σ_0 as a function of h using Eq. (3); (4) calculate the value of the generalized transition parameter, Λ, as a function of h using Eq. (8); and finally (5) using Eq. (13), determine the range of h values over which the $\Lambda < \Lambda_{\text{boundary}}(n)$. If the solution is valid for a value of h that is reasonable for the given experimental condition, then the rigid approximation can be used to calculate W_A using the measured F_p.

4.3. *Effect of the form of the interaction potential*

The Dugdale interaction model is a useful simplification that allows for a full analytical solution to the adhesive contact-mechanics problem for a tip contacting a surface (Maugis, 1992). In the previous sections it was shown, as previously described (Zheng and Yu, 2007), that once the tip geometry deviates from a paraboloid, the pull-off force depends not only on the tip geometry and work of adhesion, but also strongly on the adhesion range, h. Here we consider other types of adhesive interaction potentials and investigate the effect of the form of the potential on the pull-off force of paraboloidal and power-law-shaped tips.

Three traction-separation laws, a Lennard–Jones potential and two triangular potentials (Fig. 6), were examined. The Lennard–Jones (L–J) potential that describes the adhesive stress acting between two surfaces is

$$\sigma(d) = \frac{8W_A}{3z_0}\left[\left(\frac{z_0}{d}\right)^9 - \left(\frac{z_0}{d}\right)^3\right], \tag{14}$$

where σ is the adhesive stress, z_0 is the equilibrium separation distance at which the adhesive stress is zero, and d is the separation between two surfaces (Greenwood, 2009). This '3–9' L–J potential defines the adhesive stress between two surfaces and is determined by integrating the common '6–12' particle–particle potential over two half spaces (Muller et al., 1980). The L–J potential is related to the Dugdale potential here through two simultaneous conditions: (1) by setting $\sigma_0 = \sigma_{\max}$, where σ_0 is the constant stress in Dugdale law and, σ_{max} is the maximum attractive stress in L–J potential; and (2) by setting $W_{A,\ Dug} = W_{A,\ L\text{–}J}$, where $W_{A,\ Dug}$ is the area under the Dugdale curve, and $W_{A,\ L\text{–}J}$ is the area under the attractive portion of the L–J curve. As a result, the equilibrium separation of the L–J potential becomes $z_0 = h/0.974$. Using this relation, for a given value of h the Dugdale and L–J potentials exhibit the same maximum stress and the same work of adhesion values, although the L–J potential extends out to infinity, while the Dugdale potential becomes zero at $d = h$ (see Fig. 6).

Triangular-shaped traction-separation laws are commonly used in cohesive-zone modeling for the study of interfacial fracture (e.g., Camanho et al., 2003; Waas and De, 2006), and here we investigate two different forms. The two triangular interactions considered have the same work of adhesion, W_A, but different maximum stress values. In the first case (denoted Tri1), the adhesion range, h, is matched to that of the Dugdale interaction, and thus the maximum adhesive stress, σ_{max}, is twice that of the Dugdale interaction. For the second case (denoted Tri2), the maximum stress value was matched to that of the Dugdale interaction (namely, $\sigma_{max} = \sigma_0$), and therefore the adhesive forces extend to $2h$ (Fig. 6). Note that in the following discussion, consistent with the previous discussion and Fig. 6, h is defined as the adhesion range for the Dugdale model. Thus for Tri1, h corresponds to the separation distance beyond which the adhesive stress is zero, whereas for Tri2 the value of the adhesion stress at a separation of h is equal to σ_{max}.

The FE-calculated pull-off forces for the three interactions discussed above (L–J, Tri1, and Tri2) were compared to the M–D-n solution as a function of adhesion range (Fig. 7) for the two tip geometries defined previously in Fig. 4a and d. For

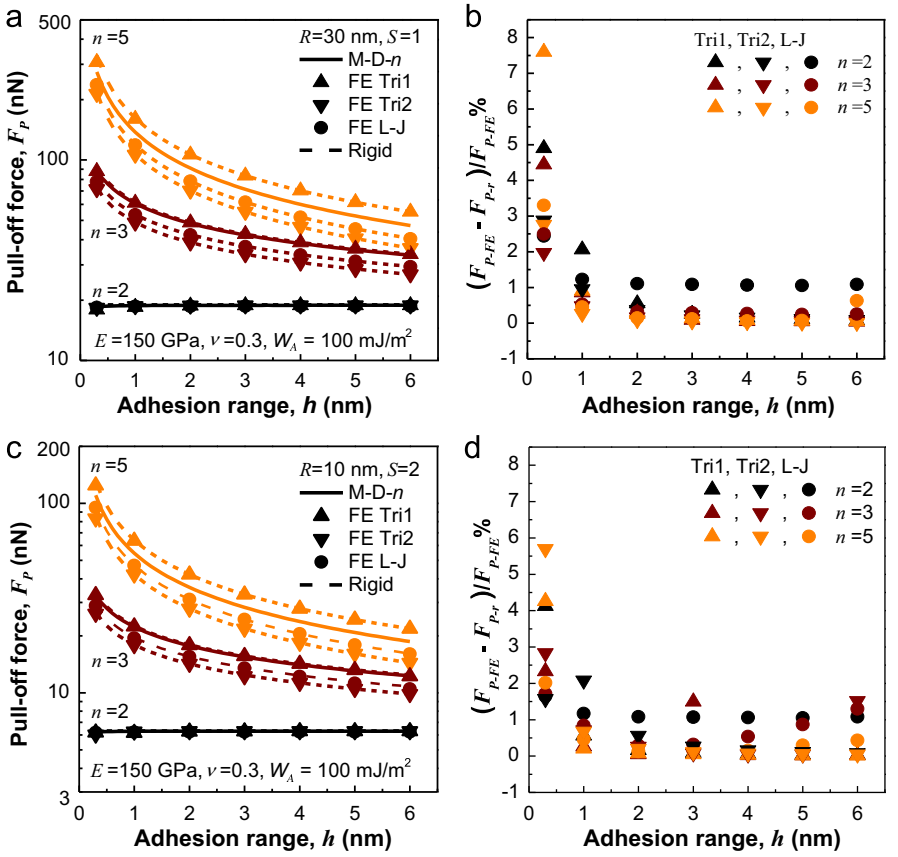

Fig. 7. (a) Comparison between the analytical M–D-n results (solid line), the FE results for Tri1 (up triangle), Tri2 (down triangle), and Lennard–Jones (circles) potentials, and the rigid results (dashed line) with $R=30$ nm. (b) Percent difference between the FE results and the rigid results in (a). (c) Comparison between the analytical M–D-n results (solid line), the FE results for Tri1 (up triangle), Tri2 (down triangle), and Lennard–Jones (circles) potentials, and the rigid results (dashed line) with $R=10$ nm. (d) Percent difference between the FE results and the rigid results in (c).

$n=2$, there is very close agreement between the pull-off forces calculated with M–D-n solution and the three FE models with different interaction potentials. However, when $n>2$, the pull-off forces differ appreciably with the form of the traction law (Fig. 7a and c). For example, for $n=5$, the results for F_P using the Tri1 potential are 17% larger than those for $F_{P\text{-}M\text{-}D\text{-}n}$, and the results for F_P using the Tri2 potential are 23% smaller than those for $F_{P\text{-}M\text{-}D\text{-}n}$. This highlights the significant influence that the interaction law has on the relationship between the work of adhesion and the pull-off force when the tip deviates from a paraboloidal shape.

Pull-off forces were also calculated using the assumption that the tip is rigid, $F_{P\text{-}r}$, through direct integration of the three interaction potentials (L–J, Tri1, and Tri2); these results are plotted as dashed lines in Fig. 7a and c. Direct integration of the triangular interaction laws yields closed-form analytical solutions,[3] while the pull-off force for the L–J interaction case was determined via numerical integration. The rigid-limit pull-off forces are in excellent agreement with the FE results for a wide range of h values (Fig. 7b and d) for the cases examined. The percent error between the rigid results and the FE results is no larger than 8%, with the percent error only exceeding 5% for the case of Tri1 with an adhesion range of 0.3 nm (Fig. 7b and d). These results again demonstrate that for a range of typical AFM contact conditions between stiff materials, the rigid-limit approximation provides a simple and effective means to interpret pull-off force measurements.

The rigid-limit approximation was used to further assess the influence of the form of the interaction potential on the pull-off force. Fig. 8 compares the rigid-limit results for the L–J and two triangular interaction potentials with the rigid Dudgale results. The results in Fig. 8 are independent of h and tip size (R and S), and are only a function of the power index, n. For the L–J and Tri1 interactions, the calculated pull-off forces are smaller than those calculated for the Dugdale interaction when n increases initially beyond 2, but converge eventually to $F_{P\text{-}r\ Dug}$ when n becomes large (i.e., when the tip becomes flat). For the Tri2 interaction, the pull-off force is slightly smaller than the Dugdale pull-off force for $2<n<3$, but becomes larger than the Dugdale pull-off force for $n>3$, converging eventually to $2F_{P\text{-}r\ Dug}$ when n becomes large. Thus in

[3] $F_{P-r,tri1} = \frac{2^{2-(2/n)}n^{1+(2/n)}W_A\pi(hR^{n-1}/(2^{2/n}-1))^{2/n}}{(2+n)h}$, $F_{P-r,tri2} = \frac{2n^{1+\frac{2}{n}}W_A\pi\left(\frac{hR^{n-1}}{2^{2/n}-1}\right)^{\frac{2}{n}}}{(2+n)h}$

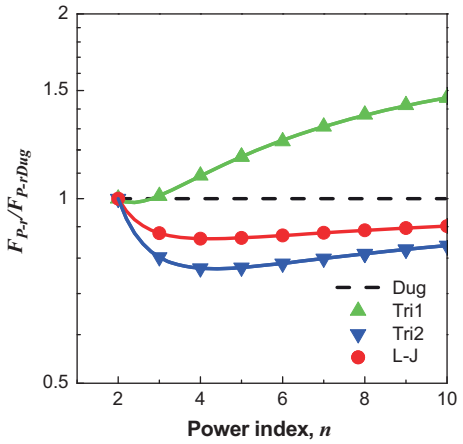

Fig. 8. Comparison between the rigid approximations of the pull-off force for the different interaction potentials as a function of the power index, n. All results are normalized by those of the rigid Dudgale results.

Table 1
Comparison of the adhesion range, h, calculated with different interaction potentials.

Adhesion range	Potential			
	Dugdale	**L–J**	**Tri1**	**Tri2**
$h_{DLC\text{-}DLC}$ (nm)	4.5–4.8	5.6–6.2	5.3–6.4	5.3–6.4
$h_{Si\text{-}DLC}$ (nm)	4.2–4.9	5.3–6.6	5.4–5.8	5.4–5.8

the *simplified case of a rigid tip and surface*, W_A governs the value of the pull-off force when the tip is paraboloidal in shape, and the maximum stress of the interaction potential determines the value of the pull-off force when the tip is flat ($n\rightarrow\infty$). The pull-off force for tips with intermediate values of n depends on W_A, σ_0, and the shape of the potential. The direct dependence of F_P on σ_0 for flat, rigid tips can be understood by recognizing that the pull-off force for a flat tip is equal to the maximum stress of the interaction potential multiplied by the area of the flat part of the tip. We note that in many previous fracture mechanics studies using traction-separation laws, the shape of the potential has been shown not to be particularly important; the fracture behavior is governed primarily by W_A and σ_0 alone (e.g., Tvergaard and Hutchinson, 1992). In the present results, W_A and σ_0 are significant parameters, but the shape of the potential also has an effect. There are important differences, however, between the study here and previous fracture mechanics studies: (1) the work here examines a limiting case where elastic deformation is severely limited or absent completely and (2) the higher-index tip-shapes examined have relatively steep profiles compared to the planar cracks typically examined in fracture mechanics problems. Both of these differences likely increase the importance of the shape of the potential in determining the behavior of the system and may explain the difference between the current results and previous fracture studies.

The analysis of experimental data in Section 3 to determine the adhesion range from measurements was repeated using the rigid results for the L–J, Tri1, and Tri2 interactions – the results are summarized in Table 1. By using the work of adhesion calculated from the paraboloid ($n=2$) tip as the reference, effective adhesion ranges were again calculated. Compared to the results of $h=4$–5 nm from the Dugdale analysis, the adhesion ranges for the L–J, Tri1 and Tri2 interactions (considering the adhesion range for Tri2 to be the full range $2h$ here) are $\sim$20% larger for both DLC and Si tips, in the range of 5.5–6.5 nm. This again highlights the important role that the tip shape and the form of the interaction potential have on the analysis and interpretation of experimental pull-off force measurements. Therefore, although the M–D-n model provides a useful, comprehensive framework for analyzing a wide range of realistic tip geometries, the assumption of a Dugdale traction-separation law may still result in errors in interpreting experimental pull-off-force measurements. Determining the most-accurate form of the interaction potential remains a challenge.

5. Conclusions

We have demonstrated and discussed techniques for analyzing AFM pull-off force measurements from tips that have a shape described by a power-law function. FE modeling results are in good agreement with the analytical M–D-n solution of Zheng and Yu (2007) and allowed the analysis to be extended to more complex interaction potentials. We also introduced a simple rigid approximation for the pull-off force and developed a map in (R/h, σ_0/E^*) space that delineates the cases in which the simplified analysis can be applied to quantify experimentally measured adhesion behavior. We find that rigid

approximations apply quite well for relating the pull-off force to the adhesion parameters over a wide range of AFM experimental conditions. We also investigated the impact that different forms of the adhesion potential have on the results for the pull-off force for power-law-shaped tips. Applying the M–D-n analysis to experimental data, an adhesion range of $\sim$4–5 nm was determined for both Si and DLC-coated AFM tips that evolved into power-law shapes due to wear. When using more sophisticated interaction potentials (e.g., a Lennard–Jones potential and triangular potentials), an adhesion range of 5.5–6.5 nm was determined. These values are all significantly higher than the typically assumed values of less than 1 nm (corresponding to the equilibrium separations for strong atomic bonds), but are physically reasonable considering other possible sources of interfacial adhesion.

These results demonstrate a unique route to quantitatively extract work of adhesion and the adhesion range from experimental measurements of pull-off forces using recently developed contact-mechanics models of power-law shaped tips. A key finding for experimentalists to keep in mind is that pull-off forces for power-law shaped tips with exponents greater than two (i.e., non-paraboloidal tips) depend on the adhesion range and, to a lesser extent, the form of the interaction potential. This behavior is considerably different from the more familiar paraboloid case (e.g., DMT, JKR) in which the pull-off force is weakly dependent on the adhesion range and is largely independent of the form of the interaction potential.

Acknowledgment

This work is supported by NSF under grants #CMMI-0825000, #CMMI-0845294, and #CMMI-0826076.

References

Bares, J.A., Sumant, A.V., Grierson, D.S., Carpick, R.W., Sridharan, K., 2007. Small amplitude reciprocating wear performance of diamond-like carbon films: dependence of film composition and counterface material. Tribol. Lett. 27, 79–88.

Bhushan, B., 2004. Springer Handbook of Nanotechnology. Springer-Verlag, Berlin.

Bloo, M.L., Haitjema, H., Pril, W.O., 1999. Deformation and wear of pyramidal, silicon-nitride AFM tips scanning micrometre-size features in contact mode. Meas.: J. Int. Meas. Confederation 25, 203–211.

Camanho, P.P., Davila, C.G., De Moura, M.F., 2003. Numerical simulation of mixed-mode progressive delamination in composite materials. J. Compos. Mater. 37, 1415–1438.

Cappella, B., Butt, H.J., Kappl, M., 2005. Force measurements with the atomic force microscope: technique, interpretation and applications. Surf. Sci. Rep. 59, 1–152.

Carpick, R.W., Agrait, N., Ogletree, D.F., Salmeron, M., 1996a. Measurement of interfacial shear (friction) with an ultrahigh vacuum atomic force microscope. J. Vac. Sci. Technol. B 14, 1289–1295.

Carpick, R.W., Agraït, N., Ogletree, D.F., Salmeron, M., 1996b. Erratum: Measurement of interfacial shear (friction) with an ultrahigh vacuum atomic force microscope [J. Vac. Sci. Technol. B 14, 1289 (1996)]. J. Vac. Sci. Technol. B 14, 2772.

Cho, J.H., Lee, D.H., Lim, J.A., Cho, K., Je, J.H., Yi, J.M., 2004. Evaluation of the adhesion properties of inorganic materials with high surface energies. Langmuir 20, 10174–10178.

Chung, K.-H., Kim, D.-E., 2003. Fundamental investigation of micro wear rate using an atomic force microscope. Tribol. Lett. 15, 135–144.

Chung, K.-H., Kim, D.-E., 2007. Wear characteristics of diamond-coated atomic force microscope probe. Ultramicroscopy 108, 1–10.

Derjaguin, B.V., Muller, V.M., Toporov, Y.P., 1975. Effect of contact deformations on the adhesion of particles. J. Colloid. Interface Sci. 53, 314–326.

Drelich, J., Tormoen, G.W., Beach, E.R., 2004. Determination of solid surface tension from particle-substrate pull-off forces measured with the atomic force microscope. J. Colloid. Interface Sci. 280, 484–497.

Frank, W.O., Daniel, W.L., Ronald, F.B., Charles, W.C., 2010. NIST Handbook of Mathematical Functions. Cambridge University Press.

Gao, H., Yao, H., 2004. Shape insensitive optimal adhesion of nanoscale fibrillar structures. Proc. Natl. Acad. Sci. U.S.A. 101, 7851–7856.

Giesbers, M., Kleijn, J.M., Cohen Stuart, M.A., 2002. Interactions between acid- and base-functionalized surfaces. J. Colloid. Interface Sci. 252, 138–148.

Gotsmann, B., Lantz, M.A., 2008. Atomistic wear in a single asperity sliding contact. Phys. Rev. Lett. 101, 125501.

Gozen, B.A., Ozdoganlar, O.B., 2010. A rotating-tip-based mechanical nano-manufacturing process: nanomilling. Nano Scale Res. Lett. 5, 1403–1407.

Greenwood, J.A., 1997. Adhesion of elastic spheres. Proc. R. Soc. London Ser. A (Math. Phys. Eng. Sci.) 453, 1277–1297.

Greenwood, J.A., 2009. Adhesion of small spheres. Philos. Mag. 89, 945–965.

Grierson, D.S., Flater, E.E., Carpick, R.W., 2005. Accounting for the JKR-DMT transition in adhesion and friction measurements with atomic force microscopy. J. Adhes. Sci. Technol. 19, 291–311.

Han, J., Yeom, J., Mensing, G., Joe, D., Masel, R.I., Shannon, M.A., 2009. Surface energy approach and AFM verification of the (CF)n treated surface effect and its correlation with adhesion reduction in microvalves. J. Micromech. Microeng., 19.

Jacquot, C., Takadoum, J., 2001. A study of adhesion forces by atomic force microscopy. J. Adhes. Sci. Technol. 15, 681–687.

Jallo, L.J., Chen, Y., Bowen, J., Etzler, F., Dave, R., 2011. Prediction of inter-particle adhesion force from surface energy and surface roughness. J. Adhes. Sci. Technol. 25, 367–384.

Johnson, K.L., Kendall, K., Roberts, A.D., 1971. Surface energy and the contact of elastic solids. Proc. R. Soc. London A Mater. 324, 301–313.

Katsuki, F., Saguchi, A., Takahashi, W., Watanabe, J., 2002. The atomic-scale removal mechanism during Si tip scratching on Si and SiO_2 surfaces in aqueous KOH with an atomic force microscope. Jpn. J. Appl. Phys. 41, 4919.

Larsen, T., Moloni, K., Flack, F., Eriksson, M.A., Lagally, M.G., Black, C.T., 2002. Comparison of wear characteristics of etched-silicon and carbon nanotube atomic-force microscopy probes. Appl. Phys. Lett. 80, 1996–1998.

Lee, D., Lee, H., Lee, N.S., Kim, K.B., Seo, Y., 2012. High-speed atomic force microscopy with phase-detection. Curr. Appl. Phys.. in press.

Leite, F.L., Herrmann, P.S.P., 2005. Application of atomic force spectroscopy (AFS) to studies of adhesion phenomena: a review. J. Adhes. Sci. Technol. 19, 365–405.

Lin, Q., Meyer, E.E., Tadmor, M., Israelachvili, J.N., Kuhl, T.L., 2005. Measurement of the long- and short-range hydrophobic attraction between surfactant-coated surfaces. Langmuir 21, 251–255.

Liu, H., Klonowski, M., Kneeburg, D., Dahlen, G., Osborn, M., Bao, T., 2005. Advanced atomic force microscopy probes: wear resistant designs. J. Vac. Sci. Technol. B 23, 3090–3093.

Liu, J., Grierson, D.S., Moldovan, N., Notbohm, J., Li, S., Jaroenapibal, P., O'Connor, S.D., Sumant, A.V., Neelakantan, N., Carlisle, J.A., Turner, K.T., Carpick, R.W., 2010a. Preventing nanoscale wear of atomic force microscopy tips through the use of monolithic ultrananocrystalline diamond probes. Small 6, 1140–1149.

Liu, J., Notbohm, J.K., Carpick, R.W., Turner, K.T., 2010b. Method for characterizing nanoscale wear of atomic force microscope tips. ACS Nano 4, 3763–3772.
Luan, B., Robbins, M.O., 2005. The breakdown of continuum models for mechanical contacts. Nature 435, 929–932.
Malshe, A.P., Rajurkar, K.P., Virwani, K.R., Taylor, C.R., Bourell, D.L., Levy, G., Sundaram, M.M., McGeough, J.A., Kalyanasundaram, V., Samant, A.N., 2010. Tip-based nanomanufacturing by electrical, chemical, mechanical and thermal processes. CIRP Ann. – Manuf. Technol. 59, 628–651.
Maugis, D., 1992. Adhesion of spheres: the JKR-DMT transition using a Dugdale model. J. Colloid. Interface Sci. 150, 243.
Maugis, D., 1995. Extension of the Johnson–Kendall–Roberts theory of the elastic contact of spheres to large contact radii. Langmuir 11, 679–682.
Maw, W., Stevens, F., Langford, S.C., Dickinson, J.T., 2002. Single asperity tribochemical wear of silicon nitride studied by atomic force microscopy. J. Appl. Phys. 92, 5103–5109.
Mo, Y., Turner, K.T., Szlufarska, I., 2009. Friction laws at the nanoscale. Nature 457, 1116–1119.
Muller, V.M., Yushchenko, V.S., Derjaguin, B.V., 1980. On the influence of molecular forces on the deformation of an elastic sphere and its sticking to a rigid plane. J. Colloid. Interface Sci. 77, 91–101.
Persson, B.N.J., 2003. Nanoadhesion. Wear 254, 832–834.
Singh, J., Whitten, J.E., 2008. Forces between polymer surfaces and self-assembled monolayers. J. Macromol. Sci. Part A: Pure Appl. Chem. 45, 885–892.
Stiess, S., Richter, A., King, B.V., Reitsma, M., Smith, R., 2004. A Lateral Force Microscopy Study of Friction Between Glassy Carbon and Different Surfaces, 8 ed. John Wiley and Sons Ltd, pp. 1246–1249.
Sumant, A.V., Grierson, D.S., Gerbi, J.E., Birrell, J., Lanke, U.D., Auciello, O., Carlisle, J.A., Carpick, R.W., 2005. Toward the ultimate tribological interface: surface chemistry and nanotribology of ultrananocrystalline diamond. Adv. Mater. 17, 1039–1045.
Tian, T., Chung-Yuen, H., 2005. Decohesion of a rigid punch from an elastic layer: transition from "flaw sensitive" to "flaw insensitive" regime. J. Polym. Sci. Part B (Polym. Phys.) 43, 3628–3637.
Tormoen, G.W., Drelich, J., Beach III, E.R., 2004. Analysis of atomic force microscope pull-off forces for gold surfaces portraying nanoscale roughness and specific chemical functionality. J. Adhes. Sci. Technol. 18, 1–17.
Tortonese, M., Kirk, M., 1997. Characterization of application specific probes for SPMs, Proceedings of SPIE – The International Society for Optical Engineering, USA, pp. 53–60.
Tvergaard, V., Hutchinson, J.W., 1992. The relation between crack-growth resistance and fracture process parameters in elastic plastic solids. J. Mech. Phys. Solids 40, 1377–1397.
Ukraintsev, V., Banke, B., 2010. Reference metrology for nanotechnology: significance, challenges and solutions, Proceedings of SPIE – The International Society for Optical Engineering, USA, p. 77670C.
Villarrubia, J.S., 1997. Algorithms for scanned probe microscope image simulation, surface reconstruction, and tip estimation. J. Res. Natl. Inst. Stand. Technol. 102, 425–454.
Waas, A.M., De, X., 2006. Discrete cohesive zone model for mixed-mode fracture using finite element analysis. Eng. Fract. Mech. 73, 1783–1796.
Wiesmann, D., Rawlings, C., Vecchione, R., Porro, F., Gotsmann, B., Knoll, A., Pires, D., Duerig, U., 2009. Multi Tbit/in2 storage densities with thermomechanical probes. Nano Lett. 9, 3171–3176.
Yao, H., Ciavarella, M., Gao, H., 2007. Adhesion maps of spheres corrected for strength limit. J. Colloid. Interface Sci. 315, 786–790.
Zheng, Z., Yu, J., 2007. Using the Dugdale approximation to match a specific interaction in the adhesive contact of elastic objects. J. Colloid. Interface Sci. 310, 27–34.